Title

Utilizing Nanoscale Particulate Matter from the Combustion of Diesel Fuels as a Carbonaceous Anode Electrode for Li-ion Batteries

Author

Cronin, Stephen B

Publication Date

2022-08-01

Data Availability

The data associated with this publication are available at:
https://doi.org/10.7910/DVN/C5ODOH

Utilizing Nanoscale Particulate Matter from the Combustion of Diesel Fuels as a Carbonaceous Anode Electrode for Li-ion Batteries

August 2022

A Research Report from the National Center for Sustainable Transportation

Stephen B. Cronin, University of Southern California

National Center for Sustainable Transportation

METRANS Transportation Center
USC | CSULB

TECHNICAL REPORT DOCUMENTATION PAGE

1. Report No. NCST-USC-RR-22-32	**2. Government Accession No.** N/A	**3. Recipient's Catalog No.** N/A
4. Title and Subtitle Utilizing Nanoscale Particulate Matter from the Combustion of Diesel Fuels as a Carbonaceous Anode Electrode for Li-ion Batteries		**5. Report Date** August 2022 **6. Performing Organization Code** N/A
7. Author(s) Stephen B. Cronin, PhD, https://orcid.org/0000-0001-9153-7687		**8. Performing Organization Report No.** N/A
9. Performing Organization Name and Address University of Southern California METRANS Transportation Center University Park Campus, VKC 367 MC:0626 Los Angeles, California 90089-0626		**10. Work Unit No.** N/A **11. Contract or Grant No.** USDOT Grant 69A3551747114
12. Sponsoring Agency Name and Address U.S. Department of Transportation Office of the Assistant Secretary for Research and Technology 1200 New Jersey Avenue, SE, Washington, DC 20590		**13. Type of Report and Period Covered** Final Report (May 2020 – May 2022) **14. Sponsoring Agency Code** USDOT OST-R

15. Supplementary Notes
Dataset DOI: https://doi.org/10.7910/DVN/C5ODOH
Originally published in *Resources, Conservation and Recycling,* Volume 177, 2022, 105972.
https://doi.org/10.1016/j.resconrec.2021.105972.

16. Abstract
According to the Environmental Protection Agency's National Emissions Inventory Report, hundreds of thousands of tons of particulate matter (PM2.5) are released by diesel combustion per year. The toxic PM2.5 air pollution causes serious public health problems and is responsible for millions of worldwide deaths each year. This study investigates the electrochemical energy storage capability of annealed soot PM originating from diesel exhaust. Soot composite electrodes were utilized as anode electrodes and cycled against Li counter electrodes. X-ray diffraction and Raman spectroscopy showed the graphitized carbon structure of the annealed soot particles. The cycle life and rate-capability of the electrodes were investigated via galvanostatic cycling tests. The electrodes exhibited excellent rate performance with discharge capacities of 235, 195, 150, 120, and 80 mAh/g when cycled at rates of 1C, 2C, 5C, 10C, and 20C, respectively. The electrode demonstrated an initial discharge capacity of 154 mAh/g at 4C rate with a capacity retention of almost 77% after 500 cycles. Raman analysis confirms the retention of structural ordering in the soot carbon after 500 cycles. Kinetic analysis, obtained through cyclic voltammetry at different scan rates, indicates pseudocapacitive charging behavior in the soot composite electrode. The study provides a viable pathway towards a sustainable energy-environment by converting an abundant toxic pollutant into a valuable electrode material for Li-ion batteries.

17. Key Words Particulate matter, Pseudocapacitive, Li-ion battery, Diesel soot, Sustainability	**18. Distribution Statement** No restrictions.		
19. Security Classif. (of this report) Unclassified	**20. Security Classif. (of this page)** Unclassified	**21. No. of Pages** 35	**22. Price** N/A

Form DOT F 1700.7 (8-72) Reproduction of completed page authorized

NCST

About the National Center for Sustainable Transportation

The National Center for Sustainable Transportation is a consortium of leading universities committed to advancing an environmentally sustainable transportation system through cutting-edge research, direct policy engagement, and education of our future leaders. Consortium members include: University of California, Davis; University of California, Riverside; University of Southern California; California State University, Long Beach; Georgia Institute of Technology; and University of Vermont. More information can be found at: ncst.ucdavis.edu.

Disclaimer

Acknowledgments

This work was supported by a start-up grant from Oklahoma State University. This work was supported in part by the Army Research Office (ARO) award no. W911NF-19-1-0257 (S.Y.). This study was funded, partially or entirely, by a grant from the National Center for Sustainable Transportation (NCST), supported by the U.S. Department of Transportation (USDOT) through the University Transportation Centers program. The authors would like to thank the NCST and the USDOT for their support of university-based research in transportation, and especially for the funding provided in support of this project.

NCST

Utilizing Nanoscale Particulate Matter from the Combustion of Diesel Fuels as a Carbonaceous Anode Electrode for Li-ion Batteries

A National Center for Sustainable Transportation Research Report

August 2022

Stephen B. Cronin, Department of Electrical and Computer Engineering, University of Southern California

NCST

[page intentionally left blank]

TABLE OF CONTENTS

List of Figures

Utilizing Nanoscale Particulate Matter from the Combustion of Diesel Fuels as a Carbonaceous Anode Electrode for Li-ion Batteries

EXECUTIVE SUMMARY

According to the Environmental Protection Agency's National Emissions Inventory Report, hundreds of thousands of tons of particulate matter ($PM_{2.5}$) are released by diesel combustion per year[1,2]. The toxic $PM_{2.5}$ air pollution causes serious public health problems and is responsible for millions of worldwide deaths each year[3]. In this study investigates the electrochemical energy storage capability of annealed soot PM originating from diesel exhaust. Soot composite electrodes were utilized as anode electrodes and cycled against Li counter electrodes. X-ray diffraction and Raman spectroscopy showed the graphitized carbon structure of the annealed soot particles. The cycle life and rate-capability of the electrodes were investigated via galvanostatic cycling tests. The electrodes exhibited excellent rate performance with discharge capacities of 235, 195, 150, 120, and 80 mAh/g when cycled at rates of 1C, 2C, 5C, 10C, and 20C, respectively. The electrode demonstrated an initial discharge capacity of 154 mAh/g at 4C rate with a capacity retention of almost 77% after 500 cycles. Raman analysis confirms the retention of structural ordering in the soot carbon after 500 cycles. Kinetic analysis, obtained through cyclic voltammetry at different scan rates, indicates pseudocapacitive charging behavior in the soot composite electrode. The study provides a viable pathway towards a sustainable energy-environment by converting an abundant toxic pollutant into a valuable electrode material for Li-ion batteries.

Introduction

The steady increase in the consumption of fossil fuels in modern society has caused several serious environmental and human health issues. The burning of fossil fuels not only produces carbon dioxide emissions, which are contributing to global warming and poisoning the world's oceans but also releases toxic air-borne pollutants into the atmosphere[4,5]. For example, the combustion of fossil fuels in diesel engines generates nanoscale particulate matter (PM) with an aerodynamic diameter lower than 2.5 µm (i.e., $PM_{2.5}$). According to the Global Burden of Disease report, almost 3.2 million worldwide deaths per year are attributed to health diseases associated with $PM_{2.5}$ air pollution, making it the 6th highest risk factor for premature mortality[3]. The long-reaching adverse effects of this PM include complications in infant development during prenatal period[6], mental illnesses[7], respiratory health[8], and cardiovascular health[9–11]. In particular, combustion-derived carbonaceous particles have been suggested in recent years to be up to 5 times more toxic than inorganic particulate compositions[12–14]. According to the Environmental Protection Agency's (EPA) 2017 National Emissions Inventory Report, approximately 123,000 tons of $PM_{2.5}$ were released by diesel combustion in the year 2017[1,2]. The combustion of diesel fuels in California alone produces more than 25,000 tons of toxic nanoscale particulate matter (PM) as a waste product every year[15]. This has captured the attention of global organizations such as the World Health Organization (WHO), which gives an average annual guideline of 10 µg/m^3 of $PM_{2.5}$ in their air quality guidelines[16]. Furthermore, this attention has prompted decision-makers such as the Environmental Protection Agency (EPA)[17], Federal-Provincial Advisory Committee[18], and the European Union[19] to impose standards on the emissions of nanoscale particulate matter. For example, the Euro 6 update limited the emission of particulate matter to 0.01 g/kWh for heavy duty engines and 0.005 g/km for light-duty vehicles operating in Europe, and further, more stringent air quality standards are expected in the future. Effective implementation of these policies is key to control and mitigate $PM_{2.5}$ air pollution[20].

Black Carbon is other name that refers to optically black combustion generated particles, especially diesel particles. Black Carbon is the second largest contributor to human-induced climate warming, after carbon dioxide. Shipping over the ocean contributes 8 to 13% of global Black Carbon emissions[21]. The arctic climate is especially vulnerable to Black Carbon deposition because of its impact on the albedo of snow, glaciers, and sea ice—accelerating melting and increasing sensitivity to warming.

These requirements have necessitated the need for an improvement in the technology restricting diesel engine particulate emissions. Diesel particulate filters (DPFs) and electrostatic precipitators (ESPs) are common methods of reducing combustion engine emissions[22–24]. However, these DPFs become clogged over extended use and must be cleaned out. If not maintained properly, these filters can exert a large back pressure on the engine ultimately reducing engine efficiency. The carbonaceous waste soot collected from these filters is of limited use and mostly ends up as industrial toxic waste. Potential commercial application of the waste material is needed to transform it into useful chemicals for sustainability. Previously, we demonstrated the application of diesel engine exhaust soot as a conductive additive for two

different Li-ion battery cathode materials, lithium manganese oxide (LMO) and lithium iron phosphate (LFP)[25]. In the study presented here, we examine the electrochemical storage capability of carbonaceous particulate matter as an anode material for Li-ion batteries.

Li-ion batteries are pervasive in modern society with applications in cell phones, laptops, and power tools. The discovery of graphite anodes in the early 1990s lead to the commercialization of rechargeable lithium-ion batteries in 1991 because graphite allows reversible Li-ion insertion (i.e., intercalation) and removal from its structure. In recent years, a number of publications have come forth with various carbonaceous electrodes as alternatives to graphite electrode from a variety of sources including prawn shells[26], corn stalk cores[27], rice husks[28], garlic peels[29], sweet potatoes[30], wheat flour[31], and soot from marine gas oil[32] among others. The porous carbon derived from these sources were exposed to the high temperature treatment, which results in a cost penalty for the production of the material. On the other hand, in this study, soot particles, collected by the electrostatic precipitation, only baked at 250 ^{o}C. Table 1 lists the carbon sources, synthesis process and electrochemical performance of the porous carbon electrodes derived from biomass resources.

Table 1. Literature survey on the synthesis and the electrochemical performance of the recycled carbon materials derived from various sources as anode in Li-ion batteries. C-rates are based on theoretical capacity of 372 mA/g.

Li or Na-ion Battery	Carbon Source	Synthesis	Discharge Capacity (mAh/g)	Current Density (mA/g)
Li-ion	Garlic Peel[29]	Baking (300 ^{o}C)+ KOH bath + Pyrolysis (850 ^{o}C for 2 hrs)	200	4000 (~10.8C)
Li-ion	Sweet patato[30]	Pyrolysis (800 ^{o}C for 4 hrs) + Autoclave	84	3720 (~10C)
Li-ion	Rice husk[28]	Autoclave + H_2SO_4 bath + Pyrolysis (600 ^{o}C for 1.5 hrs)	155	1860 (~5C)
Li-ion	soot from marine gas oil[32]	Pyrolysis (1000 ^{o}C for 1 hr)	395	3720 (~10C)
Li-ion	prawn shells[26]	Baking (300 ^{o}C)+ NaOH bath + Pyrolysis (750 ^{o}C for 2 hrs)	147	2000 (~5.4C)
Li-ion	corn stalk cores[27]	Baking (300 ^{o}C)	107	1860 (~5C)
Li-ion	corn stalk cores[27]	Baking (300 ^{o}C)+ Pyrolysis (550 ^{o}C for 4 hrs) + KOH bath	275	1860 (~5C)

Li or Na-ion Battery	Carbon Source	Synthesis	Discharge Capacity (mAh/g)	Current Density (mA/g)
Na-ion	Garlic Peel[29]	Baking (300 °C)+ KOH bath + Pyrolysis (850 °C for 2 hrs)	142	500
Na-ion	prawn shells[26]	Baking (300 °C)+ NaOH bath + Pyrolysis (750 °C for 2 hrs)	107	2000
Na-ion	Onion[33]	Baking (300 °C)+ NaOH bath + Pyrolysis (600 °C for 3 hrs)	46	2000
Na-ion	low density polyethylene bags[34]	Pyrolysis (700 °C under 3310 kPa)	92	150
Na-ion	N-doped porous carbon nanosheet[35]	KOH bath + Pyrolysis (800 °C for 2 hrs)	140	500

In this study, we investigate the electrochemical performance of soot particles derived from the combustion of diesel fuel. The morphological and chemical structure of the soot particles were characterized using SEM, XPS, and XRD analysis. The composite anode electrodes were fabricated by mixing the soot particles with conductive carbon and binder. The electrochemical behavior of the soot composite electrodes was characterized via cyclic voltammetry and impedance spectroscopy. The cycle life and rate capability of the electrode were investigated via galvanostatic cycling tests. The electrode demonstrated 150 mAh/g capacity at a 4C rate and capacity retention was almost 77% after 500 cycles. Excellent rate-capability of the soot electrode suggested pseudocapacitive charge behavior of the electrode, which was further investigated by conducting cyclic voltammetry over a wide range of scan rates and Raman spectroscopy studies.

Materials and Methods

Recycled Particulate Matter

The details of the preparation of the soot particles were explained in detail in our previous publication[25]. Briefly, soot particles were collected from diesel engine exhaust using electrostatic precipitation. The electrostatic precipitation of soot is highly energy efficient and requires less than 1% of the engine power. The preparation of soot anode material consists primarily of low-temperature annealing that could potentially be carried out using various waste heat sources. The collected particles were then annealed at 250 oC in the argon environment for 4 hours. We performed high resolution transmission electron microscopy (HRTEM) imaging of the unannealed (Figure 8) and annealed (Figure 9). Both samples show crystal lattice fringes corresponding to roughly 3.4Å spacing, indicating

graphitic structure. According to these images, there is no apparent difference in the material structure with and without annealing. Gas chromatography/mass spectrometry (GC/MS) during the annealing process is shown in Figure 10 of the Supplemental Document. The temperature was scanned from 50 Celsius to 300 Celsius, while GC/MS spectra were taken. As the temperature increased, the emergence of a CO2 increased with temperature. The absence of any other species observed at later retention times (i.e., 4–12 minutes) indicates that there are no substantial hydrocarbons emitted during this annealing process.

Electrode Fabrication

Annealed diesel soot particles were used as the active material in composite electrodes for electrochemical characterizations. The composite electrodes were fabricated by mixing the annealed soot particles with carboxymethyl cellulose sodium salt binder (CMC, Aldrich) and Super P® conductive carbon additive (Alfa Aesar) in an 8:1:1 mass ratio, respectively. CMC was chosen as a binder because the electrode undergoes less irreversible deformations due to the formation of solid-electrolyte interface when CMC is used as a binder for carbonaceous Li-ion anodes compared to the PVDF binder[36]. First, the CMC binder was dissolved in ultrapure water and mixed for 10 min in a Thinky centrifugal mixer at 2000 rpm mixing speed. Next, the annealed soot particles and Super P® conductive carbon were added to the binder mixture. The resulting slurry was mixed in a Thinky centrifugal mixer at 2000 rpm for 30 minutes. The slurry was then cast onto Cu foil (9 µm thick, >99.99%, MTI) using a doctor blade.

Electrochemical Cycling

CR2032 coin cells were assembled using the composite electrode as a working electrode, Li foil (99.9% metal basis, Alfa Aesar) as a counter electrode, and Celgard polyethylene film as a separator. The electrolyte was prepared by dissolving 1 M $LiClO_4$ in 1:1 (v:v) ethylene carbonate (EC, anhydrous, 99%, Sigma Aldrich): dimethyl carbonate (DMC, anhydrous, >99%, Sigma Aldrich). Coin cell assembly and electrolyte preparation were both performed in a glovebox under an inert argon atmosphere with moisture and oxygen levels kept below 1.5 ppm. Galvanostatic cycling and cyclic voltammetry tests were conducted between 2.0 to 0.01 V vs $Li^{+/0}$ on an Arbin potentiostat/galvanostat (MSTAT21044). Lithiation refers to the insertion of Li^+ ions into the composite electrode during the discharge cycle, and delithiation refers to the extraction of Li^+ ions from the composite electrode during the charge cycle.

During galvanostatic cycling, a constant current, I, is applied until the cell potential reaches the set minimum (0.01 V) or maximum (2.0 V) value. The C-rates in galvanostatic cycling were calculated using Faraday's law: $C-rate = \frac{Qm_{sp}}{I}$, where the theoretical capacity of graphite, Q is 372 mAh/g and m_{sp} denotes a mass of annealed soot particles in the composite electrode[36]. In all galvanostatic tests, coin cell batteries were first cycled 3 times to allow the formation of solid-electrolyte interface (SEI) layers. The capacity retention and rate capability of the soot composite electrode were then investigated by conducting galvanostatic cycle experiments at

various rates. The experiments were performed at least twice, and the average values based on repeated experiments are presented in the paper.

During cyclic voltammetry, the cell potential was increased and decreased at a constant rate (μV/s) between 0.01 and 2.0 V vs $Li^{+/0}$. Cyclic voltammetry experiments were performed at different rates (between 25 and 2500 μV/s) to investigate the charging mechanism of Li ions into annealed soot particles. Electrochemical impedance spectroscopy (EIS) was conducted on the pristine and cycled cells using a Biologic potentiostat equipped with EC-lab® acquisition software.

Structural and Morphological Characterization

X-ray diffraction (XRD) patterns were captured using a Bruker D8 Advance XRD with Lynxeye Detector. A Witec alpha300 Raman microscope was used to identify carbon-related bands using a 532nm laser and a 50x objective lens with a power of 2.5-3.5 mW and integration time of 2.5s. X-ray photoelectron spectroscopy (XPS) measurements were taken with a Kratos Axis Ultra DLD spectrometer.

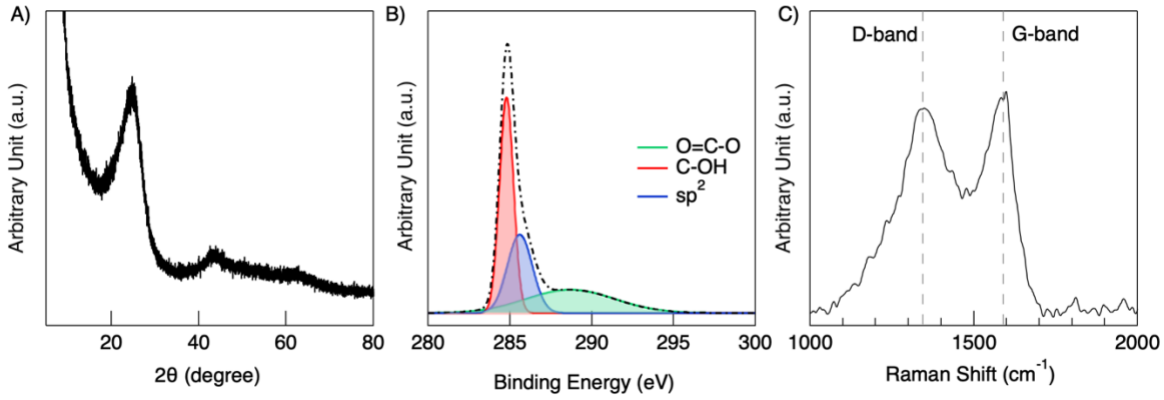

Figure 1. Characterization of Material Chemistry: A) XRD analysis of annealed soot powders, B) XPS spectrum of annealed soot powder, C) Raman spectrum of pristine soot

Results and Discussion

Material Characterization

The structure and chemical composition of the diesel soot particles were characterized by using high resolution transmission electron microscope (HRTEM), powder X-ray diffraction (XRD), Raman spectroscopy, and X-ray photoelectron spectroscopy (XPS) measurements. The crystal structure of the annealed soot particles was investigated using XRD, as shown in Figure 1A. It is a well-known phenomenon that the high number of structural defects in the layered structure of graphite produces strong distortions of the diffraction peaks[37,38]. This distortion cannot be avoided as it is an intrinsic feature of graphitized carbon. Despite this distortion, two diffraction peaks were observed near 24.7° and 43.8°, corresponding to the (002) diffraction peak for

parallel graphene sheets and the (100) peak from the covalently bonded structure of carbon atoms within each graphene sheet, respectively[39]. These results suggest the presence of graphitized carbon in the structure of annealed soot particles. High-resolution XPS C1s spectra are shown in Figure 1B. The C1s spectrum is found to be a combination of three peaks at 285, 286, and 289 eV, which correspond to sp^2 C–C, C–OH, and O=C–O bonds, respectively[26,40–42]. The areal percentage of these peaks was calculated, and the percentage of sp^2 C–C, C–OH, and O=C–O peaks were found to be 43.0, 27.8, and 29.2%, respectively.

The Raman spectra of the pristine soot composite electrode are shown in Figure 1C. The presence of two peaks, a D-band at ~1350 cm^{-1} and a G-band at ~1580cm^{-1}, is a distinctive feature of graphitized carbon. The first peak, at ~1340 cm^{-1} is caused by the A_{1g} vibration associated with defects in the aromatic rings and can be attributed to amorphization of the carbon structure[43]. The second peak at ~1580^{-1} is caused by the E_{2g} vibration of the sp^2 hybridized carbon atoms. The ratio of the intensity of these two peaks (I_D/I_G) is commonly used to evaluate the degree of disorder present in graphitized carbon[44,45]. For the pristine soot composite electrodes, the I_D/I_G ratio was measured to be 0.94. The average particle size of the soot particles was measured to be around 20-30 nm[25].

Electrochemical Behavior of Soot Composite Electrode

The electrochemical properties of the soot composite electrodes were evaluated using a variety of electrochemical experiments, as shown in Figure 2. First, cyclic voltammetry (CV) was performed to investigate reversible and irreversible electrochemical reactions during the initial cycles[46]. During CV, the potential changes linearly with time at a constant rate between the two cutoff voltages. Figure 2A shows the current evolution during the first five cycles of CV between 0.01–2.0 V vs $Li/Li^{0/+}$ at a scan rate of 200 μV s^{-1}. During the first cathodic scan (i.e., potential sweep from higher potential to lower potential), a broader current peak was detected at 1.26 and 0.76 V. These peaks disappeared in the subsequent cycle, indicating that they are due to the formation of the solid-electrolyte interface (SEI) on the electrode from electrolyte decomposition[47]. Irreversible reduction current peaks were detected for various carbonaceous electrodes during the first cycle due to the electrolyte decomposition[48,49]. For carbonaceous electrodes, the cathodic peak between 0.01-0.2V is associated with reversible Li-ion intercalation, and the anodic peak at around 0.25 V results from Li-ion extraction from the host structure[30]. Similar electrochemical behavior is observed for the soot composite anode in Fig. 10A. A reversible and sharp cathodic peak was observed around 0.01 V in the first five cycles, associated with the lithiation of the soot composite electrode. During the anodic scan (i.e., increasing from lower potential to higher potential), a broad and reversible current peak was detected around 0.25 V in the first five cycles, indicating delithiation of the electrode. Interestingly, the current profile of the electrode beyond the first cathodic cycle demonstrates a quasi-rectangular shape without pronounced redox peaks, indicating that the electrode material may possess a considerable pseudocapacitive contribution to charge storage[50]. We will discuss the capacitive behavior of the electrode by performing cyclic voltammetry at different scan rates in a later section of this manuscript.

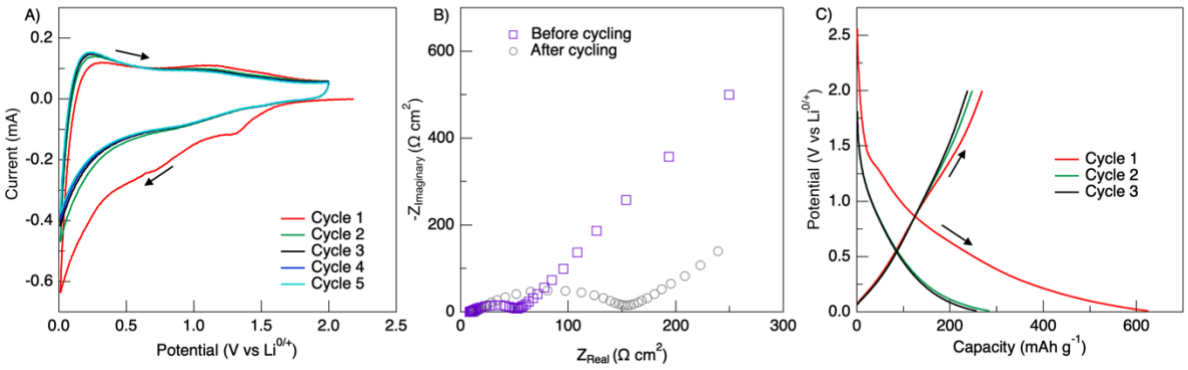

Figure 2. Electrochemical behavior of soot composite anode. A) Cyclic voltammetry at 200 µV/s for 5 cycles, B) Electrochemical impedance spectra of the composite electrode before and after 5 cycles cyclic voltammetry at 200 µV/s, C) Potential – capacity profiles during the first 3 galvanostatic cycles at C/2 rate.

Electrochemical impedance spectroscopy (EIS) is a common method for quantifying the relationship between current and voltage in an electrochemical cell through an equivalent circuit that represents physical processes occurring in the cell. EIS was applied to the composite electrode before and after cyclic voltammetry measurements, as shown in Figure 2B. The purpose of the EIS measurement is to investigate changes in cell resistance. The surface resistance is associated with the electron transfer reaction occurring on the electrode's surface and it has a direct relationship with the radius of the real impedance portion of the semicircle. The radius of the semi-circle increased from 50.9 Ω/cm^2 before cycling to 150.7 Ω/cm^2 after five cycles. This increase indicates a higher resistance to the electron transfer reaction occurring on the electrode and can be attributed to increased resistance to Li^+ diffusion through the surface film caused by the formation and growth of the SEI layer[51].

The charge/discharge capacity of the electrode was analyzed by performing galvanostatic measurements at a C/2 rate for the first 3 cycles, as shown in Figure 2C. C-rates are calculated based on the theoretical capacity of graphite (372 mAh/g). The composite electrodes display a large first cycle lithiation capacity of 625.3 mAh g^{-1}, which quickly reduced to 285 and 257 mAh g^{-1} during the 2nd and 3rd lithiation cycles, respectively. During the first discharge cycle, the slope of the potential vs capacity curve changes dramatically at around 1.25 V. This observation further supports the contribution of SEI growth on the large discharge capacity in the first cycle. The large discharge capacity drop between the first and second cycles is attributed to the formation of an SEI layer on the electrode surface[52]. It also agrees well with the increase in the resistance in Figure 2B. The delithiation capacities during the first three cycles were 268, 247, and 237 mAh g^{-1}, respectively. Beyond the first discharge cycle, the potential–capacity curves show an almost linear relationship. This is in contrast to traditional graphite anodes which display a series of plateaus during galvanostatic cycling, caused associated by the phase transformations between different stages of graphite during (de)lithiation[37]. A quasi-linear relationship between potential and capacity in the soot composite electrode suggests the capacitive behavior of the electrode, which will be discussed later.

Rate Capability

The rate-capability of the soot composite electrodes was tested by performing galvanostatic cycling at different rates. Figure 3A shows the charge/discharge capacities and Coulombic efficiencies at 1 C, 2 C, 5 C, 10 C, and 20 C-rates. The electrode was cycled for five consecutive cycles at each scan rate. The electrodes display excellent rate performance with charge capacities of 233, 194, 150, 118, and 82 mAh g-1 during the first cycle at C-rates of 1C, 2C, 5C, 10C, and 20C, respectively. Additionally, when the C-rate was restored to its initial value of 1C, a capacity of 229 mAh/g was retained which demonstrates the high reversibility of the charge storage. Compared to the literature listed in the Table 1, the composite soot electrode demonstrates very competitive performance. The potential–capacity plots for different scan rates are shown in Figure 3B.

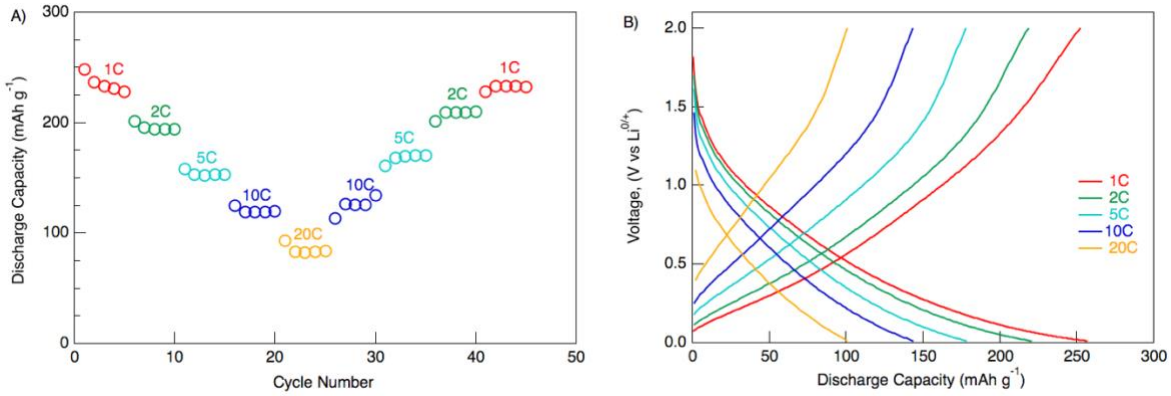

Figure 3. A) Rate performance of the electrode cycled at different C-rates, B) Potential – Capacity curves for charge and discharge cycles at different C-rates.

The potential curves retain their shape with respect to capacity at various rates, and the potential profiles lack any distinct voltage plateaus, further indicating the capacitive charge storage mechanisms in addition to Li-ion intercalation[37,53].

Cycle Life of the Soot Composite Electrode

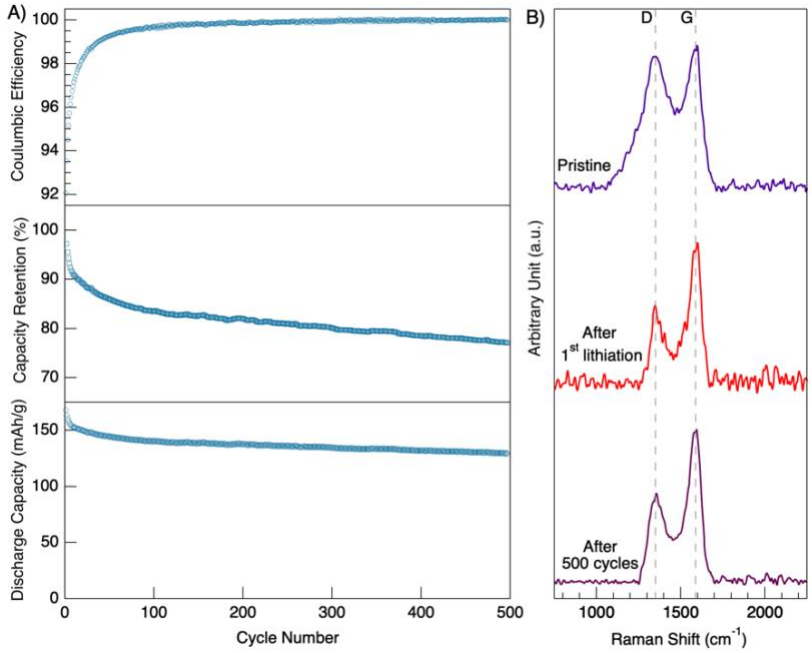

Figure 4. A) Columbic efficiency, capacity retention, and discharge capacity of the soot composite electrode cycled 4C for 500 cycles. B) Raman spectra of the electrode taken before cycling, after 1st lithiation and after 500 cycles.

The cycle life of the soot composite electrodes was tested by performing long-term galvanostatic cycling. Figure 4A shows the average charge/discharge capacities, capacity retention, and Coulombic efficiency for soot electrodes cycled at a 4C rate for 500 cycles. Before the cycle life testing, the electrode was charged/discharged three times for SEI formation and stabilization. The initial charge and discharge capacities of the electrode were 168 and 154 mAh/g, respectively, but decreased steadily throughout the initial 10-15 cycles. The charge and discharge capacities became reversible at 148 and 152 mAh/g after 15 cycles, respectively. The capacity retention was calculated by taking the ratio of the capacity at the current cycle over the first cycle: $Capacity\ retention = \frac{Q_n}{Q_1} \times 100\%$. The discharge capacity retention was about 90% by cycle 10 and decreased to 80% when the electrode was cycled 300 times, indicating highly reversible Li-ion storage ability of the soot composite anode. The Coulombic efficiency was calculated as the ratio between charge extracted (delithiation, Q_{charge}) to charge inserted (lithiation, $Q_{discharge}$) for each cycle: $CE = \frac{Q_{charge}}{Q_{discharge}} \times 100\%$. The Coulombic efficiency rose steadily over cycling from its initial value and reaches 99.99% by cycle 500. Complimentary Raman analysis was conducted to better understand the high-capacity retention in the soot composite electrode. Figure 4B shows the Raman spectra of the pristine electrode, electrode after 1st lithiation and electrode after 500 cycles. The ratio of I_D/I_G decreased after the first lithiation, demonstrating an increase in ordering of the soot carbon

with Li intercalation. The I_D/I_G ratio does not change significantly between after 1st lithiation and after 500 cycles, indicating that structural ordering is retained in the soot carbon[54].

Charging Kinetics of Li+ in Soot Composite Anode

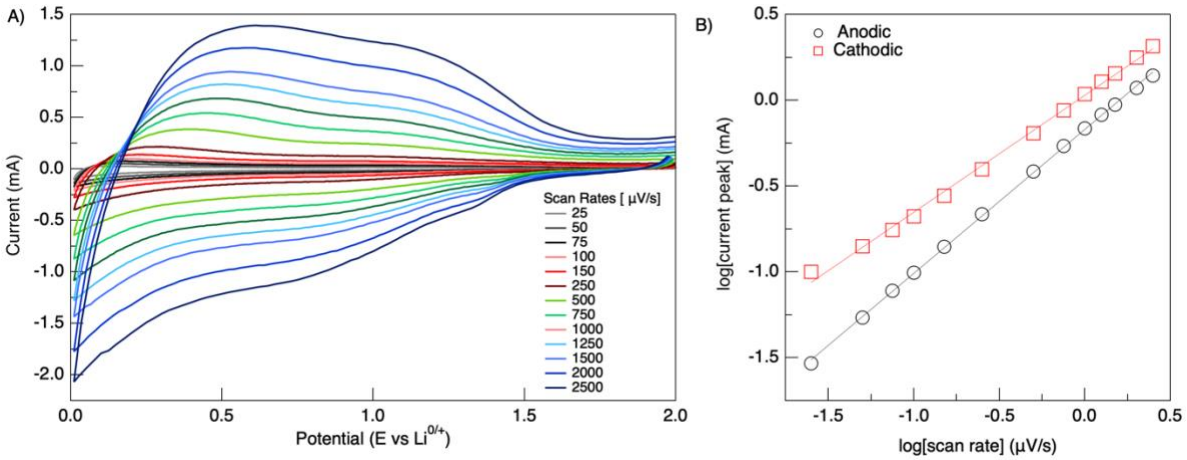

Figure 5. Li+ charge storage mechanisms in soot composite electrode. A) CV curves of the electrode at various scan rates from 25–2500 µV/s. B) Relationship between current peak and scan rate.

Cyclic voltammetry experiments were conducted at various scan rates to investigate the kinetics of lithium-ion storage in the soot composite electrode. Previous research efforts have utilized cyclic voltammetry to interrogate whether the charge storage mechanism in a material is based on intercalation or capacitive behavior[55–57]. By conducting CV at different scan rates, the difference in reaction kinetics between intercalation (which is diffusion-limited) and capacitive mechanisms can be exploited to ascertain their contributions to charge storage. The current response of the soot composite electrode cycled at a range of scan rates from 25–2500 µV/s is shown in Figure 5A. We can quantify the diffusion-controlled and surface capacitive-controlled contributions through the application of the following power-law relationship between current and scan rate:

$$i = av^b \qquad \text{Eqn. 1}$$

where *i* is peak current, *v* is the scan rate, and *a* and *b* are fitting parameters[32,42]. If the *b*-value is equal to 0.5, it indicates diffusion-controlled process charge storage behavior. On the other hand, if the *b*-value is equal to 1.0, then it suggests surface-capacitive controlled charge behavior in the electrode. Plots of $\log(|i|)$ vs $\log(|v|)$ were generated from the CV data, and the slopes of lines fitted to the data were taken as the *b*-values for the peak currents in the cathodic and anodic sweeps (Figure 5B).

Based on these power-law fits, the *b*-values for the anodic and cathodic peaks were 0.84 and 0.68, respectively. These values suggest a combination of diffusion-controlled and surface-capacitive controlled mechanisms for the lithium-ion storage in the soot composite electrode.

Further separation of the diffusion-controlled and pseudocapacitive mechanisms of charge storage was accomplished using the method of Dunn et al[58]. At each potential in the CV curve, there is a current contribution from both the intercalation and surface-controlled electron transfer reactions. The insertion process is diffusion-limited and will vary with the square root of the scan rate according to the equation

$$i = nFAC^{*}D^{\frac{1}{2}}\left(\frac{\alpha nF}{RT}\right)^{\frac{1}{2}}\pi^{\frac{1}{2}}\chi(bt)v^{1/2} \quad \text{Eqn. 2}$$

where *n* is the number of electrons involved in the electron transfer reaction, *F* is the Faraday constant, *A* is the surface area of the electrode, C^{*} is the surface concentration of the electrode material, *D* is the chemical diffusion coefficient, α is the charge transfer coefficient, *R* is the ideal gas constant, *T* is the temperature, and χ(*bt*) is a function representing the normalized current for an irreversible system. In contrast, the surface-controlled mechanism will be directly proportional to the scan rate according to the following equation:

$$i = C_D A v \quad \text{Eqn. 3}$$

where C_D is the capacitance. At a fixed potential, the contribution of the diffusion-limited and capacitive processes on the current can be defined as:

$$i(V) = k_1 v + k_2 v^{0.5} \quad \text{Eqn. 4}$$

where k_1 and k_2 represent the capacitive and interaction contributions, respectively[50]. Therefore, if values of k_1 and k_2 are found over the range of potentials in the CV, then the individual contribution of each process can be identified. To assist with this, Eqn. 4 was re-arranged into the form:

$$\frac{i(V)}{v^{0.5}} = k_1 v^{0.5} + k_2 \quad \text{Eqn. 5}$$

which allows for calculating k_1 and k_2 values from linear fits of i(V)/$v^{0.5}$ vs $v^{0.5}$ plots, where k_1 is the slope and k_2 is the y-intercept in Figure 12 at various potentials. The k_1 and k_2 values produced from the graphs in Figure 5A are provided in Table 2 alongside the R^2 value of the line fit to the data points. These values are used to calculate the current produced from the capacitive processes according to the following equation:

$$i_{cap}(V) = k_1 v \quad \text{Eqn. 6}$$

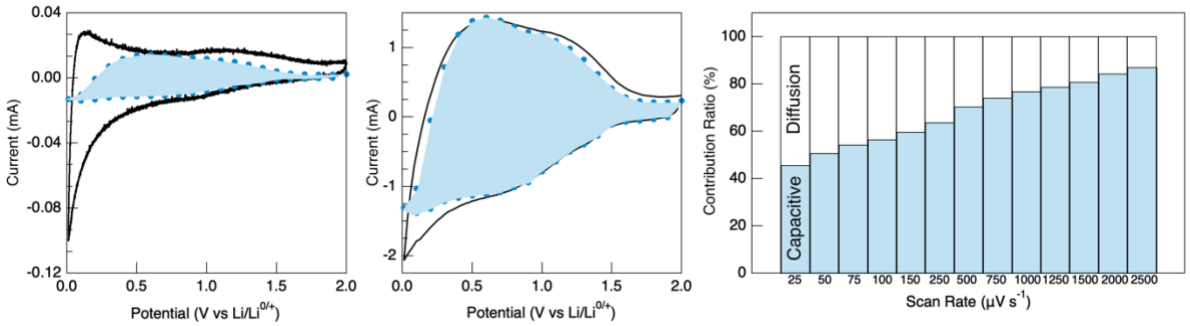

Figure 6. A, B) Current response (black straight line) and Capacitive charge storage contributions (colored with blue) at 25 and 2500 µV/s, respectively. C) Contribution ratio of diffusion-limited and capacitive factors on the charge storage at scan rates between 25.- 2500 µV/s.

The contribution of capacitive behavior to the current is plotted on top of the experimentally recorded current profiles when the electrode is cycled at 25 and 2500 µV/s in Figure 6A and Figure 6B. Contributions of the capacitive charge storage are also presented for the other scan rates in Figure 13. Figure 6C illustrates the overall contribution of capacitive and diffusion-controlled processes on the discharge capacity of the electrode at various scan rates. The relative contribution is calculated by numerically approximating the area under the curve of the overall current response and the capacitive current response using the trapezoidal rule at each scan rate and dividing the area of the capacitive current response by the overall current response, as follows: $relative\ contribution = \frac{A_{capacitive}}{A_{overall}} * 100\%$. At the slowest scan rate of 25 µV/s, the capacitive contribution is about 45.8% of the total charge storage, indicating that insertion is the primary contributor to the charge storage at this rate. However, with increasing the scan rate, the capacitive contribution significantly increases to account for 87.1% of the total charge storage when cycled at 2500 µV/s. The intercalation of Li ions into the electrode structure is a diffusion-controlled process. The pseudocapacitive mechanism involves the adsorption of ions onto the electrode surface alongside an accompanying faradaic charge transfer. As a result, the surface-capacitive charge storage mechanism has much faster kinetics than the diffusion-controlled intercalation of Li ions into the annealed soot particles[50,53]. For this reason, the capacitive charge storage mechanism provides a larger contribution to charge storage at faster scan rates.

Performance of Soot Composite Anode in Na-ion Batteries

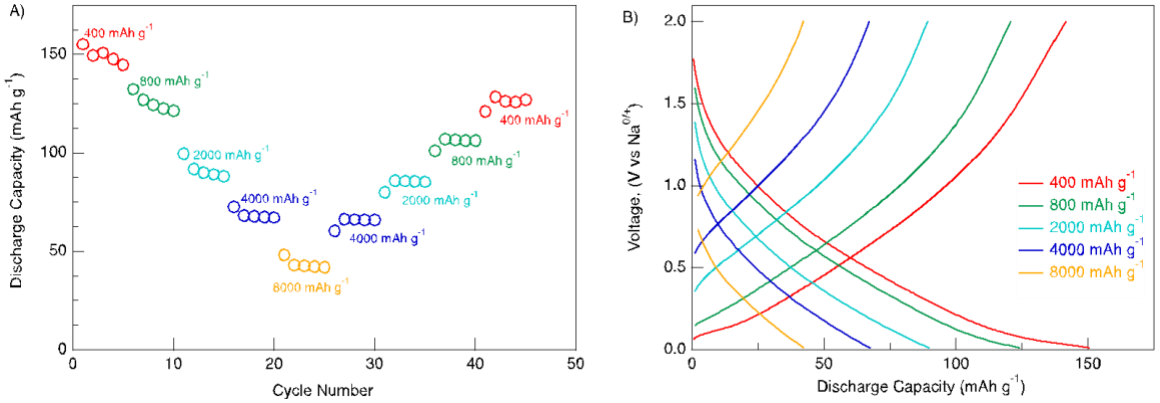

Figure 7. A) Rate performance of the electrode cycled at different C-rates for Na-ion storage, B) Potential – Capacity curves for charge and discharge cycles at different C-rates. The electrolyte was 1 M NaClO4 in EC:DMC electrolyte and the soot composite electrode was cycled against Na counter electrode.

We also investigated the ability of the soot electrode to store Na-ions as an anode electrode. The soot electrode was cycled against sodium counter electrode in 1M $NaClO_4$ in EC:DMC electrolyte. The charge/discharge capacity of the soot composite electrode in Na-ion battery at various rates was analyzed by applying constant current densities of 400, 800, 2000, 4000 and 8000 mA/g (Figure 7A). The electrode was cycled for five consecutive cycles at each constant current density. The discharge capacity of the electrode was 155, 132, 99, 72 and 48 mAh/g when discharged at constant current density of 400, 800, 2000, 4000 and 8000 mA/g, respectively. The discharge capacity reduced to 126 mAh/g when the applied current density was 400 mA/g at the cycle number 45. Compared to the literature listed in Table 1, the composite soot electrode demonstrates much better discharge capacity at similar scan rates for Na-ion batteries. The potential–capacity plots for different scan rates for Na-ion storage are shown in Figure 7B. The potential curves retain their shape with respect to capacity at various rates. Similar to Li-ion storage in Figure 3B, the potential profiles in Figure 7A lack any distinct voltage plateaus, further indicating the capacitive charge storage mechanism for Na-ions too.

Suggestions for Future Directions

In this study, we demonstrated the ability of the soot composite electrode to store Li-ion and Na-ions in Li-ion and Na-ion batteries, respectively. Due to its ability to store charge in Li-ion and Na-ion chemistries, we are curious about its ability to store other metal-ions. The pseudocapacitive behavior of the soot composite electrodes should be further investigated in various electrolyte solutions in order to further optimize its performance. We also emphasize that future research should also focus on the manufacturing ability of the soot composite electrodes at larger scale because of the low bulk density of soot particulates. In this study, the soot particulates were collected from diesel engine exhaust. A significant amount of the soot particulate matter is also generated from ships[59] and airplanes[60], which uses heavy crude oil

and kerosene as a fuel in their engine, respectively. Further studies on the collection of particulate matter from these engines as well as their potential to store charge as battery electrodes is necessary to mitigate the release of toxic soot particulates from aviation and sea-transportation.

Conclusion

In summary, we report the ability of annealed diesel soot particulate matter to store Li^+ ions as an anode electrode in Li-ion batteries. The structure and chemical composition of the annealed soot particles were characterized by X-ray diffraction, Raman spectroscopy, and X-ray photoelectron spectroscopy. The electrochemical behavior of the soot composite electrode was investigated by performing cyclic voltammetry, impedance spectroscopy, and galvanostatic cycling. The soot composite electrode demonstrated highly reversible discharge capacities when cycled at fast rates up to 20C. The electrode also demonstrated a remarkable capacity retention (77% after 500 cycles) with an initial discharge capacity of 154 mAh/g when cycled at a 4C rate. Raman analysis on the cycled electrode shed light on structural retention of the soot electrode after 500 cycles. Cyclic voltammetry analysis at different scan rates demonstrated the pseudo-capacitive behavior of the soot electrode, which provided remarkable rate ability for fast charging.

The remarkable electrochemical performance of soot composite electrodes suggests new directions to ensure the provision of energy and protecting the environment at the same time. Although there has been promising progress on electric vehicles, many other transportation vehicles such as Naval ships, large trucks, trains, and airplanes are still heavily dependent on fossil fuels with different variety of chemical impurities. The utilization of waste products from the combustion of fuels from these vehicles into valuable products for electrochemical storage devices can reduce the release of toxic materials into the earth's atmosphere and can promote the development of new electrode materials for energy storage devices.

References

1. Environmental Protection Agency. 2017 National Emissions Inventory Report. (2020).
2. Hammer, M. S. *et al.* Global Estimates and Long-Term Trends of Fine Particulate Matter Concentrations (1998-2018). *Environ. Sci. Technol.* **54**, 7879–7890 (2020).
3. Apte, J. S., Marshall, J. D., Cohen, A. J. & Brauer, M. Addressing Global Mortality from Ambient PM2.5. *Environ. Sci. Technol.* **49**, 8057–8066 (2015).
4. Pinguelli-Rosa, L. & Kahn-Ribeiro, S. The present, past, and future contributions to global warming of CO2 emissions from fuels. *Clim. Change* **48**, 289–308 (2001).
5. Oberschelp, C., Pfister, S. & Hellweg, S. Globally Regionalized Monthly Life Cycle Impact Assessment of Particulate Matter. *Environ. Sci. Technol.* **54**, 16028–16038 (2020).
6. Laine, J. E. *et al.* Prenatal Exposure to Multiple Air Pollutants, Mediating Molecular Mechanisms, and Shifts in Birthweight. *Environ. Sci. Technol.* **54**, 14502–14513 (2020).
7. Shi, W. *et al.* Depression and Anxiety Associated with Exposure to Fine Particulate Matter Constituents: A Cross-Sectional Study in North China. *Environ. Sci. Technol.* **54**, 16006–16016 (2020).
8. Zhang, J. *et al.* Chronic Exposure to PM 2.5 Nitrate, Sulfate, and Ammonium Causes Respiratory System Impairments in Mice . *Environ. Sci. Technol.* (2021). doi:10.1021/acs.est.0c05814
9. Douglas W. Dockery, et al. An association between air pollution and mortality in 6 U.S. Cities. *The New England Journal of Medicine* **329**, 1753–1759 (1993).
10. Oberdörster, G., Oberdörster, E. & Oberdörster, J. Nanotoxicology: An emerging discipline evolving from studies of ultrafine particles. *Environ. Health Perspect.* **113**, 823–839 (2005).
11. Pope III, C. A. *et al.* Lung Cancer, Cardiopulmonary Mortality, and Long-term Exposure to Fine Particulate Air Pollution. *J. Am. Med. Assoc.* **287**, 1132–1141 (2002).
12. Lelieveld, J., Evans, J. S., Fnais, M., Giannadaki, D. & Pozzer, A. The contribution of outdoor air pollution sources to premature mortality on a global scale. *Nature* **525**, 367–371 (2015).
13. Tuomisto, J. T., Wilson, A., Evans, J. S. & Tainio, M. Uncertainty in mortality response to airborne fine particulate matter: Combining European air pollution experts. *Reliab. Eng. Syst. Saf.* **93**, 732–744 (2008).
14. Shi, J., Xu, C., Xiang, L., Chen, J. & Cai, Z. Tris(2,4-di- tert-butylphenyl)phosphate: An Unexpected Abundant Toxic Pollutant Found in PM2.5. *Environ. Sci. Technol.* **54**, 10570–10576 (2020).
15. California Air Resources Board. *California's Plan to Reduce Diesel Particulate Matter Emissions.* (2010).

16. World Health Organization, W. WHO Air quality guidelines for particulate matter, ozone, nitrogen dioxide and sulfur dioxide: Global update 2005. 1–21 (2005). doi:10.1016/0004-6981(88)90109-6

17. U.S. EPA. Policy Assessment for the Review of the Particulate Matter National Ambient Air Quality Standards. *U.S. Environ. Prot. Agency, Off. Air Qual. Plan. Stand.* (2020).

18. Health Canada, E. C. National Ambient Air Quality Objectives for Particulate Matter: Executive Summary: Part 1: Science Assessment Document. *Air Qual.* (2004).

19. Union, E., Regulation, E. C., Iv, E., Iv, E. & Vi, T. E. Euro IV, Euro V and VI Emissions Regulations for Heavy Duty Vehicle Information Note. **2009**, 1–11 (2016).

20. Peng, W. *et al.* The Critical Role of Policy Enforcement in Achieving Health, Air Quality, and Climate Benefits from India's Clean Electricity Transition. *Environ. Sci. Technol.* **54**, 11720–11731 (2020).

21. Azzara, A., Minjares, R. & Rutherford, D. *Needs and opportunities to reduce black carbon emissions from maritime shipping*. *The International Council on Clean Transportation* (2015). doi:10.1016/j.atmosenv.2009.04.059

22. Boichot, R., Bernis, A. & Gonze, E. Agglomeration of diesel particles by an electrostatic agglomerator under positive DC voltage: Experimental study. *J. Electrostat.* **66**, 235–245 (2008).

23. Sudrajad, A. & Yusof, A. F. Review of electrostatic precipitator device for reduce of diesel engine particulate matter. *Energy Procedia* **68**, 370–380 (2015).

24. Walter, R., Neumann, J. & Hinrichsen, O. Extended Model for Filtration in Gasoline Particulate Filters under Practical Driving Conditions. *Environ. Sci. Technol.* **54**, 9285–9294 (2020).

25. Yang, S. *et al.* Recycling diesel soot nanoparticles for use as activated carbon in Li ion batteries. *Resour. Conserv. Recycl.* **169**, (2021).

26. Elizabeth, I., Singh, B. P., Trikha, S. & Gopukumar, S. Bio-derived hierarchically macro-meso-micro porous carbon anode for lithium/sodium ion batteries. *J. Power Sources* **329**, 412–421 (2016).

27. Li, Y., Li, C., Qi, H., Yu, K. & Liang, C. Mesoporous activated carbon from corn stalk core for lithium ion batteries. *Chem. Phys.* **506**, 10–16 (2018).

28. Yu, K. *et al.* Preparation of porous carbon anode materials for lithium-ion battery from rice husk. *Mater. Lett.* **253**, 405–408 (2019).

29. Selvamani, V., Ravikumar, R., Suryanarayanan, V., Velayutham, D. & Gopukumar, S. Garlic peel derived high capacity hierarchical N-doped porous carbon anode for sodium/lithium ion cell. *Electrochim. Acta* **190**, 337–345 (2016).

30. Zheng, P. *et al.* Sweet potato-derived carbon nanoparticles as anode for lithium ion battery. *RSC Adv.* **5**, 40737–40741 (2015).

31. Lim, D. G. *et al.* Lithium storage in structurally tunable carbon anode derived from sustainable source. *Carbon N. Y.* **121**, 134–142 (2017).

32. Baek, H. M., Kim, D. Y., Lee, W. J. & Kang, J. Application of soot discharged from the combustion of marine gas oil as an anode material for lithium ion batteries. *RSC Adv.* **10**, 36478–36484 (2020).

33. Zhao, G. *et al.* Sulphur-doped carbon nanosheets derived from biomass as high-performance anode materials for sodium-ion batteries. *Nano Energy* **67**, (2020).

34. Pol, V. G. *et al.* Spherical Carbon as a New High-Rate Anode for Sodium-ion Batteries. *Electrochim. Acta* **127**, 61–67 (2014).

35. Wang, H. G. *et al.* Nitrogen-doped porous carbon nanosheets as low-cost, high-performance anode material for sodium-ion batteries. *ChemSusChem* **6**, 56–60 (2013).

36. Jones, E. M. C., Çapraz, Ö. Ö., White, S. R. & Sottos, N. R. Reversible and Irreversible Deformation Mechanisms of Composite Graphite Electrodes in Lithium-Ion Batteries. *J. Electrochem. Soc.* **163**, A1965–A1974 (2016).

37. Missyul, A., Bolshakov, I. & Shpanchenko, R. XRD study of phase transformations in lithiated graphite anodes by Rietveld method. *Powder Diffr.* **32**, S56–S62 (2017).

38. Shi, H., Reimers, J. N. & Dahn, J. R. Structure-refinement program for disordered carbons. *J. Appl. Crystallogr.* **26**, 827–836 (1993).

39. Yang, J. *et al.* Enhanced Capacity and Rate Capability of Nitrogen/Oxygen Dual-Doped Hard Carbon in Capacitive Potassium-Ion Storage. *Adv. Mater.* **30**, (2018).

40. Selvamani, V., Ravikumar, R., Suryanarayanan, V., Velayutham, D. & Gopukumar, S. Garlic peel derived high capacity hierarchical N-doped porous carbon anode for sodium/lithium ion cell. *Electrochim. Acta* **190**, 337–345 (2016).

41. Baek, H. M., Kim, D. Y., Lee, W. J. & Kang, J. Application of soot discharged from the combustion of marine gas oil as an anode material for lithium ion batteries. *RSC Adv.* **10**, 36478–36484 (2020).

42. Liu, L. *et al.* Understanding of the Ultrastable K-Ion Storage of Carbonaceous Anode. *Adv. Funct. Mater.* **28**, 1–9 (2018).

43. Ferrari, A. C. & Basko, D. M. Raman spectroscopy as a versatile tool for studying the properties of graphene. *Nat. Nanotechnol.* **8**, 235–246 (2013).

44. Niu, F. *et al.* MoSe2-Covered N,P-Doped Carbon Nanosheets as a Long-Life and High-Rate Anode Material for Sodium-Ion Batteries. *Adv. Funct. Mater.* **27**, 1–11 (2017).

45. Ma, G. *et al.* Phosphorus and oxygen dual-doped graphene as superior anode material for room-temperature potassium-ion batteries. *J. Mater. Chem. A* **5**, 7854–7861 (2017).

46. Elgrishi, N. *et al.* A Practical Beginner's Guide to Cyclic Voltammetry. *J. Chem. Educ.* **95**, 197–206 (2018).

47. Tabassum, H. *et al.* A Universal Strategy for Hollow Metal Oxide Nanoparticles Encapsulated into B/N Co-Doped Graphitic Nanotubes as High-Performance Lithium-Ion Battery Anodes. *Adv. Mater.* **30**, (2018).

48. Penki, T. R., Shanmughasundaram, D., Kishore, B. & Munichandraiah, N. High rate capability of coconut kernel derived carbon as an anode material for lithium-ion batteries. *Adv. Mater. Lett.* **5**, 184–190 (2014).

49. Kim, M. S. *et al.* Ultra-high Li storage capacity achieved by hollow carbon capsules with hierarchical nanoarchitecture. *J. Mater. Chem.* **21**, 19362–19367 (2011).

50. Augustyn, V., Simon, P. & Dunn, B. Pseudocapacitive oxide materials for high-rate electrochemical energy storage. *Energy Environ. Sci.* **7**, 1597–1614 (2014).

51. Aurbach, D. *et al.* Common Electroanalytical Behavior of Li Intercalation Processes into Graphite and Transition Metal Oxides. *J. Electrochem. Soc.* **145**, 3024–3034 (1998).

52. Frackowiak, E., Gautier, S., Gaucher, H., Bonnamy, S. & Beguin, F. Electrochemical storage of lithium multiwalled carbon nanotubes. *Carbon N. Y.* **37**, 61–69 (1999).

53. Jiang, Y. & Liu, J. Definitions of Pseudocapacitive Materials: A Brief Review. *Energy Environ. Mater.* **2**, 30–37 (2019).

54. Cohn, A. P. *et al.* Durable potassium ion battery electrodes from high-rate cointercalation into graphitic carbons. *J. Mater. Chem. A* **4**, 14954–14959 (2016).

55. Brezesinski, T., Wang, J., Tolbert, S. H. & Dunn, B. Ordered mesoporous α-MoO3 with iso-oriented nanocrystalline walls for thin-film pseudocapacitors. *Nat. Mater.* **9**, 146–151 (2010).

56. Yang, C. *et al.* Metallic Graphene-Like VSe2 Ultrathin Nanosheets: Superior Potassium-Ion Storage and Their Working Mechanism. *Adv. Mater.* **30**, 1–8 (2018).

57. Chao, D. *et al.* Pseudocapacitive Na-Ion Storage Boosts High Rate and Areal Capacity of Self-Branched 2D Layered Metal Chalcogenide Nanoarrays. *ACS Nano* **10**, 10211–10219 (2016).

58. Wang, J., Polleux, J., Lim, J. & Dunn, B. Pseudocapacitive contributions to electrochemical energy storage in TiO 2 (anatase) nanoparticles. *J. Phys. Chem. C* **111**, 14925–14931 (2007).

59. Particulate matter - Green Ship of The Future : Green Ship of The Future. Available at: https://greenship.org/about/emission-wiki/particulate-matter/. (Accessed: 23rd August 2021)

60. Jasiński, R., Pielecha, J. & Markowski, J. Emission of particulate matter during aircraft landing operation. doi:10.1051/2016

Data Summary

Products of Research

Figure 1. Characterization of Material Chemistry: A) XRD analysis of annealed soot powders, B) XPS spectrum of annealed soot powder, C) Raman spectrum of pristine soot

Figure 2. Electrochemical behavior of soot composite anode. A) Cyclic voltammetry at 200 µV/s for 5 cycles, B) Electrochemical impedance spectra of the composite electrode before and after 5 cycles cyclic voltammetry at 200 µV/s, C) Potential – capacity profiles during the first 3 galvanostatic cycles at C/2 rate.

Figure 3. A) Rate performance of the electrode cycled at different C-rates, B) Potential – Capacity curves for charge and discharge cycles at different C-rates.

Figure 4. A) Columbic efficiency, capacity retention, and discharge capacity of the soot composite electrode cycled 4C for 500 cycles. B) Raman spectra of the electrode taken before cycling, after 1st lithiation and after 500 cycles.

Figure 5. Li+ charge storage mechanisms in soot composite electrode. A) CV curves of the electrode at various scan rates from 25–2500 µV/s. B) Relationship between current peak and scan rate.

Figure 6. A, B) Current response (black straight line) and Capacitive charge storage contributions (colored with blue) at 25 and 2500 µV/s, respectively. C) Contribution ratio of diffusion-limited and capacitive factors on the charge storage at scan rates between 25.- 2500 µV/s.

Figure 7. A) Rate performance of the electrode cycled at different C-rates for Na-ion storage, B) Potential – Capacity curves for charge and discharge cycles at different C-rates. The electrolyte was 1 M NaClO4 in EC:DMC electrolyte and the soot composite electrode was cycled against Na counter electrode.

Figure 8. HRTEM images of unannealed soot particles.

Figure 9. HRTEM images of annealed soot particles.

Figure 10. (a) Gas chromatography/mass spectrometry (GC/MS) during the annealing process, (b) CO2 signal plotted as a function of annealing temperature.

Figure 11. Capacity retention of the soot composite anode when cycled at 1 C rate against Li counter metal.

Figure 12. Relationships between i(V)/v0.5 vs v0.5 for calculating constants k1 and k2 at potentials between A) 0.01–0.5 V, B) 0.6–1.0 V, C)1.1–1.5 V, D) 1.6–2.0 V.

Figure 13. Capacitive charge storage contributions at A) 50, B) 75, C) 100, D) 150, E) 250, F) 500, G) 750, H) 1000, I)1250, J) 1500, K) 2000 µV s-1

Data Format and Content

All text is in Doc files and all figures are in PDF and origin.

Data Access and Sharing

Replication Data for: Utilizing Nanoscale Particulate Matter from the Combustion of Diesel Fuels as a Carbonaceous Anode Electrode for Li-ion Batteries is available at https://doi.org/10.7910/DVN/C5ODOH.

Reuse and Redistribution

Access to databases and associated software tools generated under the project was made available for educational, research and non-profit purposes. Such access was provided using web-based applications, as appropriate. Results generated under the project were disseminated in accordance with University/Participating institutional policies. Depending on such policies, materials were transferred to others under the terms of a material transfer agreement. The results of the research performed under this proposal were disseminated primarily through publication in peer reviewed journals and conference presentations. Periodic updates on the research were posted on the group websites. Research data that documents, supports and validates research findings were made available after the main findings from the final research data set were accepted for publication. Such research data was redacted to prevent the disclosure of personal identifiers.

Supporting Information

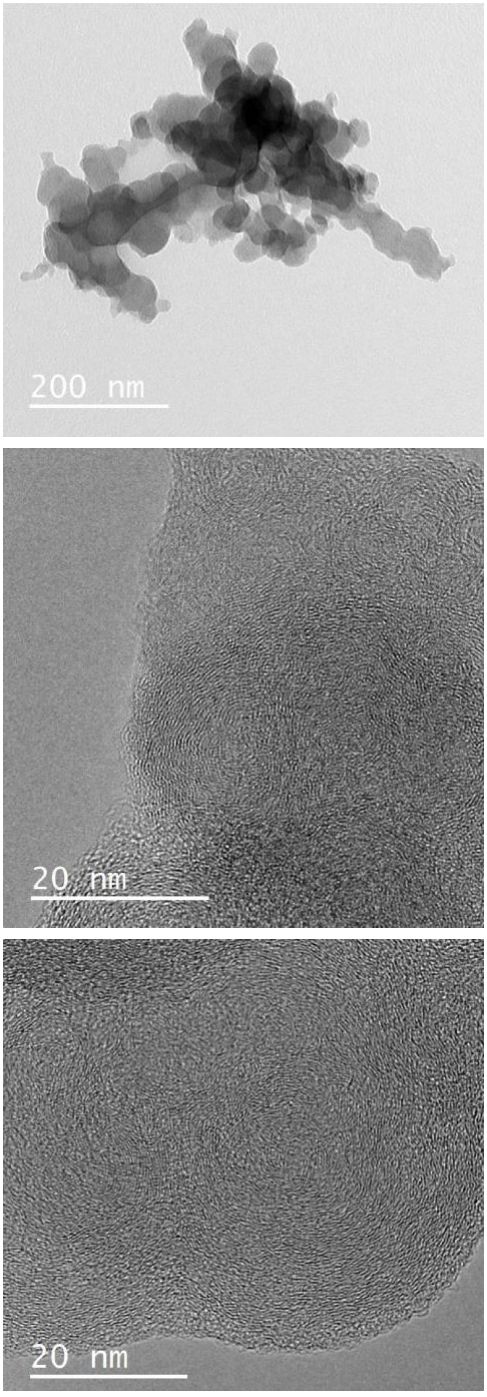

Figure 8. HRTEM images of unannealed soot particles.

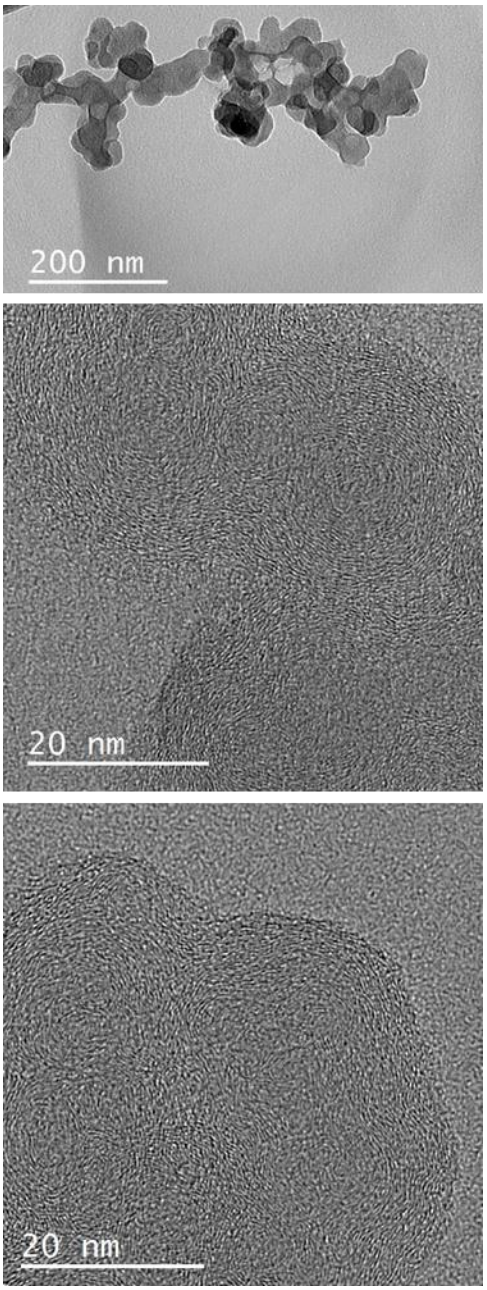

Figure 9. HRTEM images of annealed soot particles.

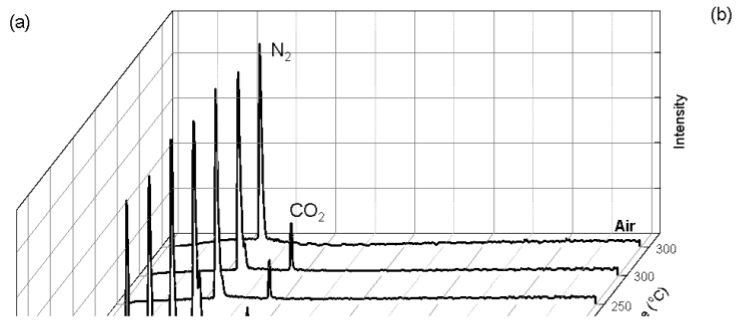

Figure 10. (a) Gas chromatography/mass spectrometry (GC/MS) during the annealing process, (b) CO2 signal plotted as a function of annealing temperature.

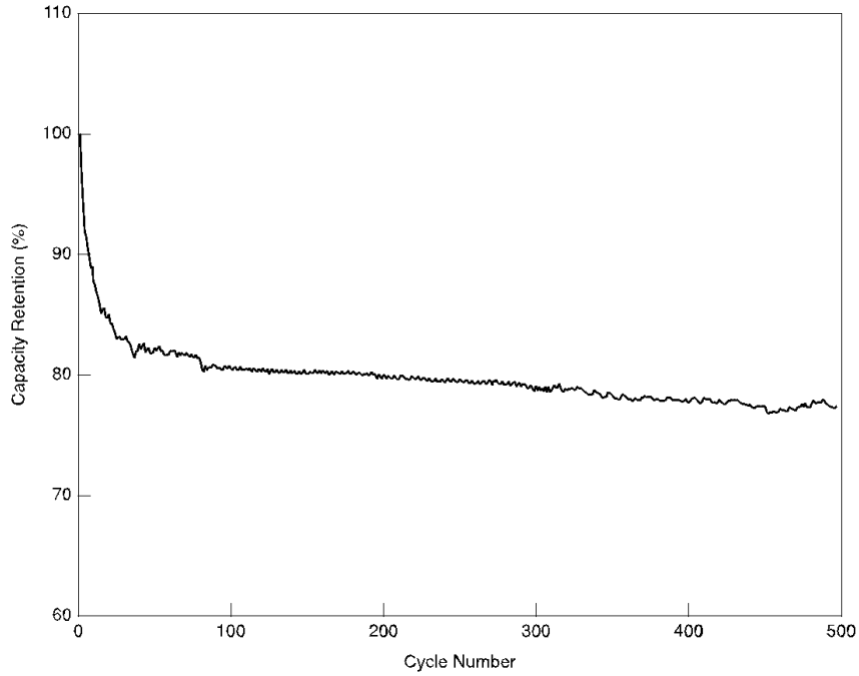

Figure 11. Capacity retention of the soot composite anode when cycled at 1 C rate against Li counter metal.

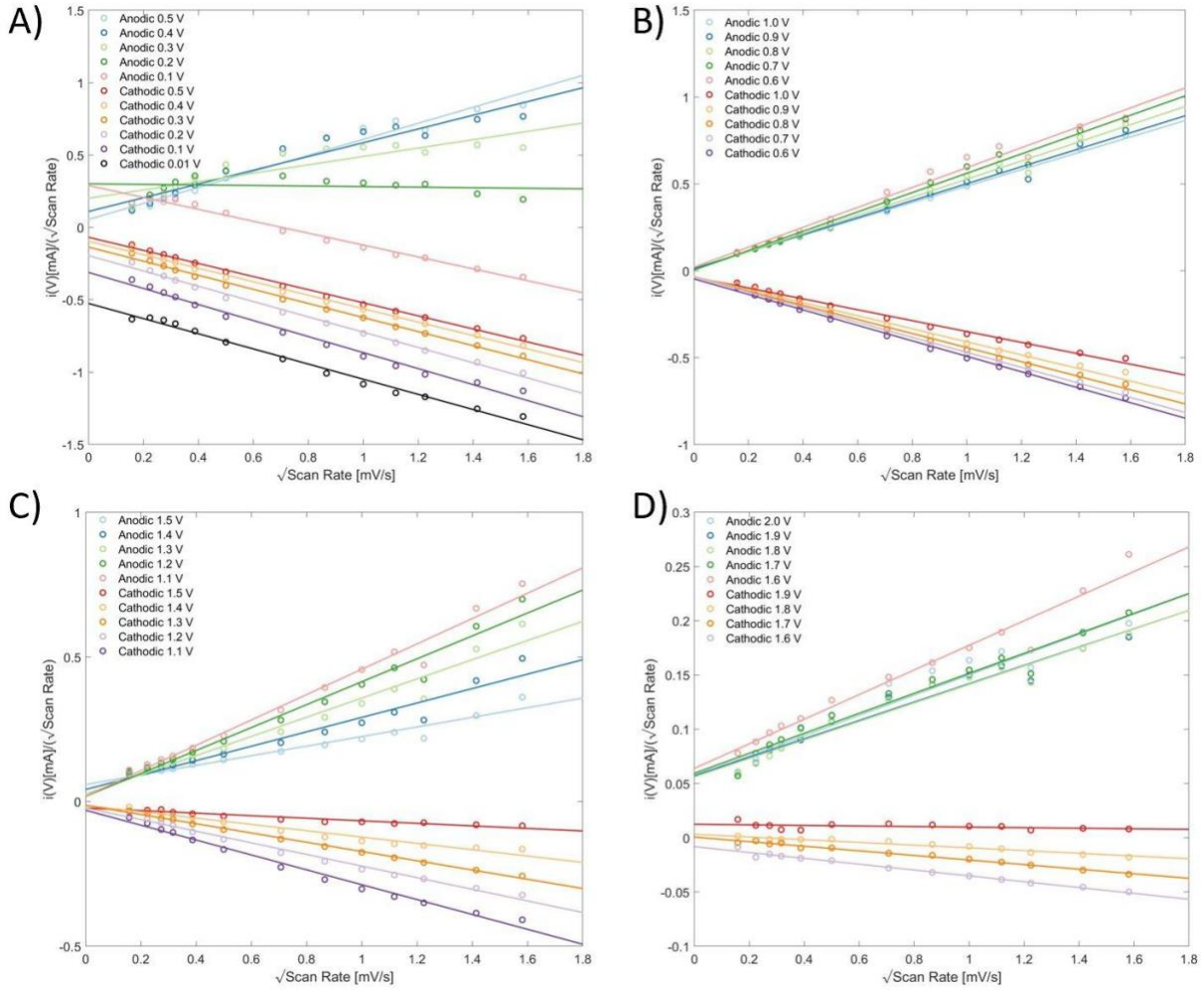

Figure 12. Relationships between i(V)/v0.5 vs v0.5 for calculating constants k1 and k2 at potentials between A) 0.01–0.5 V, B) 0.6–1.0 V, C)1.1–1.5 V, D) 1.6–2.0 V.

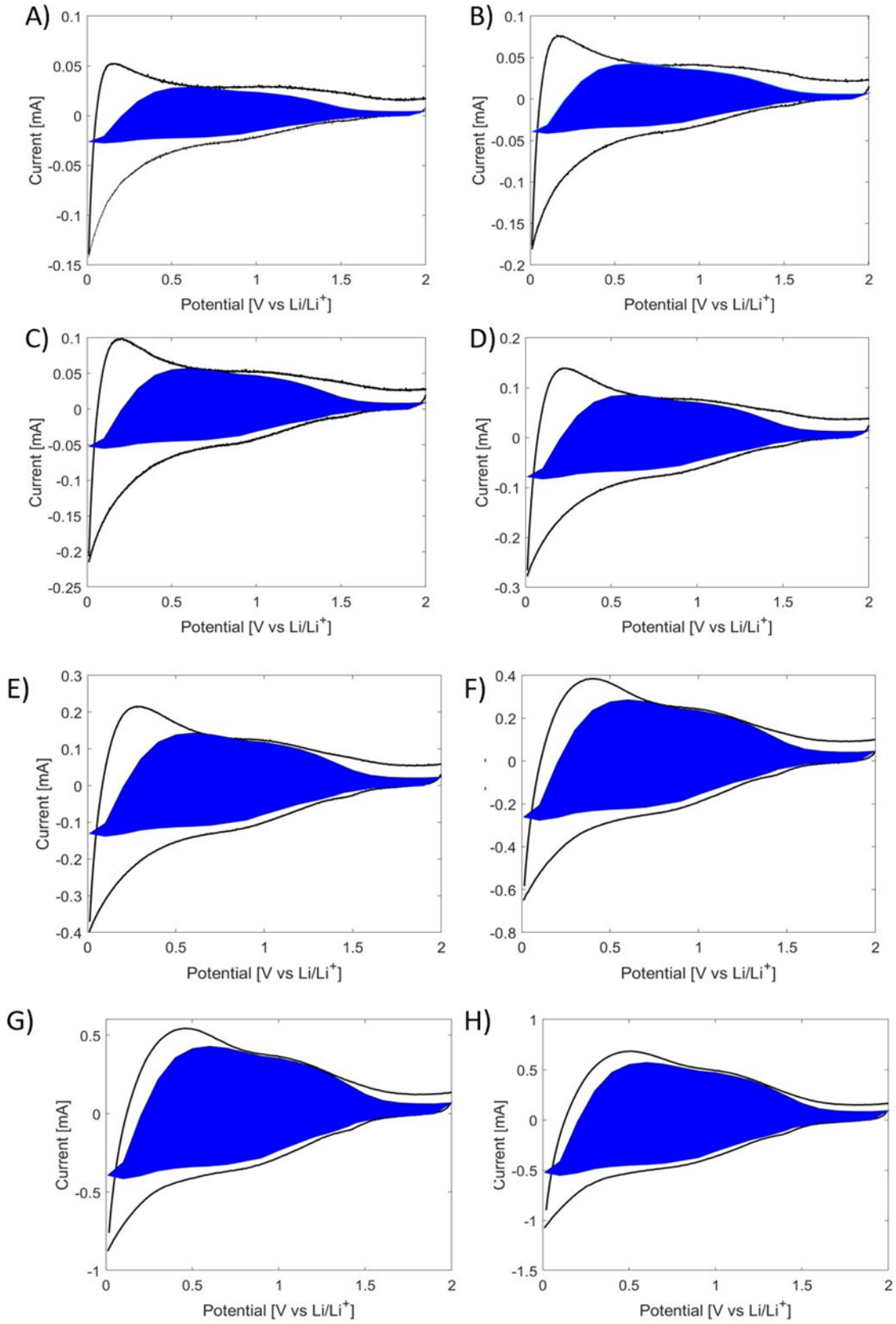
A)
B)
C)
D)
E)
F)
G)
H)
Current [mA]
Potential [V vs Li/Li+]

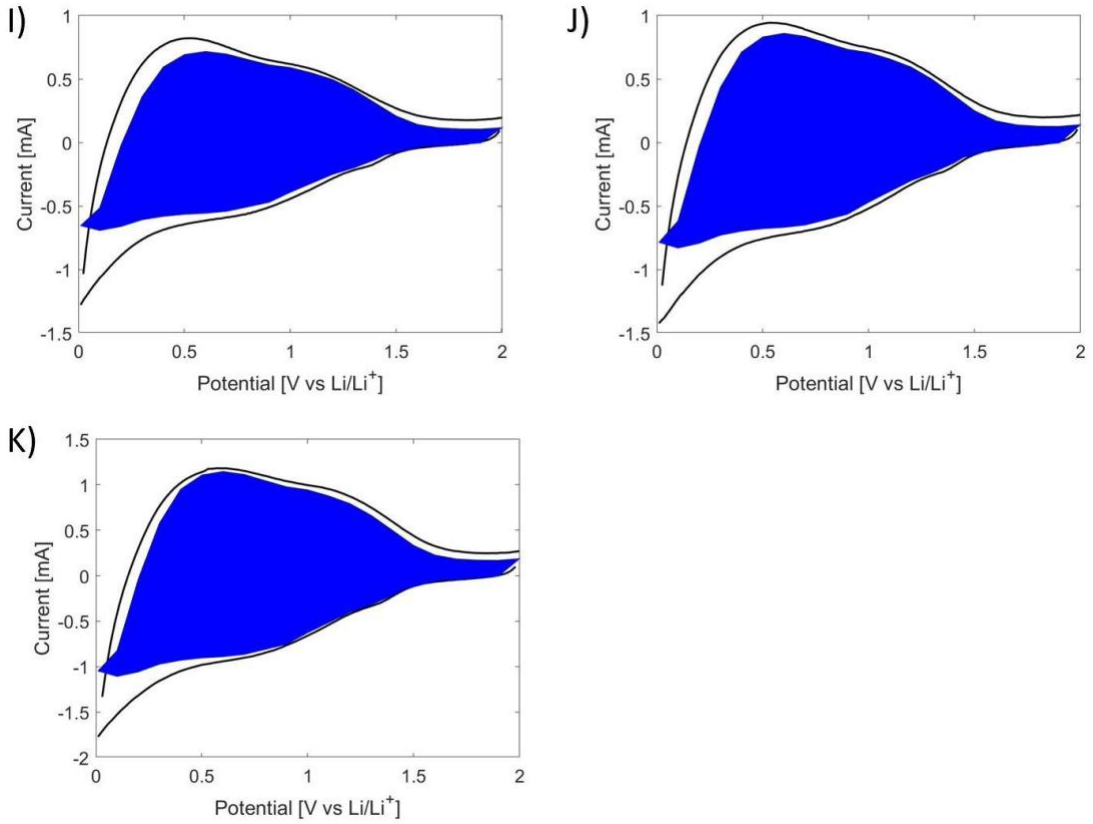

Figure 13. Capacitive charge storage contributions at A) 50, B) 75, C) 100, D) 150, E) 250, F) 500, G) 750, H) 1000, I)1250, J) 1500, K) 2000 µV s-1

Table 2. K-Values

K-Values							
Cathodic				Anodic			
Potential [V]	k1	k2	R^2	Potential [V]	k1	k2	R^2
0.01	-0.5239	-0.5254	0.9894	0.01			
0.1	-0.5541	-0.3112	0.9887	0.1	-0.4115	0.2891	0.9835
0.2	-0.5291	-0.1951	0.9949	0.2	-0.019	0.3007	0.019
0.3	-0.4867	-0.1363	0.9957	0.3	0.2893	0.2008	0.7782
0.4	-0.4652	-0.0965	0.9963	0.4	0.4752	0.1097	0.9246
0.5	-0.4524	-0.0687	0.9969	0.5	0.5537	0.0545	0.9592
0.6	-0.4456	-0.0465	0.997	0.6	0.5731	0.0209	0.9807
0.7	-0.4333	-0.0359	0.9973	0.7	0.5568	0.0048	0.9883
0.8	-0.4053	-0.0367	0.9959	0.8	0.5223	0.0055	0.9879
0.9	-0.3767	-0.0322	0.9959	0.9	0.4888	0.0127	0.9867
1	-0.3135	-0.0361	0.9922	1	0.4718	0.016	0.9893
1.1	-0.2572	-0.0299	0.9882	1.1	0.4382	0.0193	0.981
1.2	-0.2007	-0.022	0.9895	1.2	0.3961	0.0182	0.9738
1.3	-0.1598	-0.0126	0.9968	1.3	0.3315	0.0264	0.9588
1.4	-0.1092	-0.0133	0.96	1.4	0.2492	0.0419	0.9469
1.5	-0.044	-0.0223	0.9171	1.5	0.1662	0.0588	0.954
1.6	-0.0269	-0.0082	0.9837	1.6	0.1134	0.0639	0.9646
1.7	-0.0211	0.0006	0.9878	1.7	0.0921	0.0594	0.961
1.8	-0.0125	0.0032	0.9424	1.8	0.0852	0.0561	0.9608
1.9	-0.0026	0.0124	0.1978	1.9	0.0845	0.0574	0.9567
2				2	0.0934	0.0567	0.9473